THE JOURNAL OF PHYSICAL CHEMISTRY C
A JOURNAL OF THE AMERICAN CHEMICAL SOCIETY

pubs.acs.org/JPCC

Article

Neural Network-Based Interatomic Potential for the Study of Thermal and Mechanical Properties of Siliceous Zeolites

Luca Brugnoli,* Maxime Ducamp, and François-Xavier Coudert*

Cite This: *J. Phys. Chem. C* 2024, 128, 20512−20522

Read Online

ACCESS | Metrics & More | Article Recommendations | Supporting Information

ABSTRACT: Molecular dynamics simulations of zeolites are commonly employed for the characterization of their framework dynamics and response to the application of temperature and pressure. While classical interatomic potentials are commonly used for this task, they offer a description of the interactions in the system with limited accuracy. Density functional theory, meanwhile, is accurate, but its high computational expense limits its scalability for large systems or long dynamics. Recent advances in machine learning interatomic potentials, trained on computational data obtained at the quantum chemical level, offer a promising alternative combining high accuracy with computational efficiency. In this study, we developed an MLIP specifically for pure silica zeolites, trained on data from high-temperature ab initio MD simulations across various zeolitic topologies. This MLIP was then applied to predict structural properties, thermal expansion, and pressure response of different zeolites, demonstrating its potential for accuracy and generalizability in simulations of topologies beyond its initial training set.

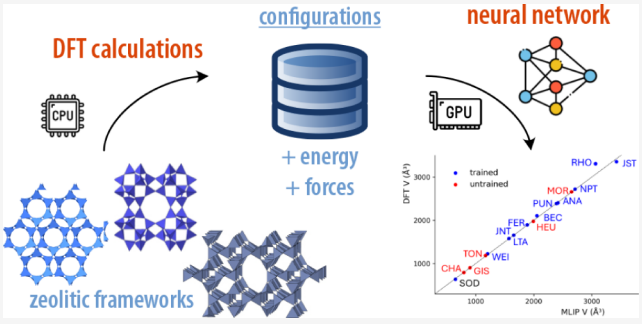

1. INTRODUCTION

Zeolites are a family of natural and artificial porous aluminosilicates that rank among the most widely produced crystalline nanoporous materials in the chemical industry, where they are used, in particular, for their active role in catalysis, adsorption, and ion exchange. Computational modeling plays a key role in understanding their fundamental properties, linking their physical and chemical behavior at the macroscopic scale to their structure and dynamics at the atomic scale. With this goal, different levels of chemical description have been used in molecular dynamics (MD) simulations of zeolites, ranging from classical interatomic potentials − with low accuracy but high transferability − to first-principles or ab initio schemes based on density functional theory (DFT), which feature high accuracy along with high computational expense. While DFT calculations are feasible on relatively small zeolitic systems, their high CPU cost makes them unsuitable for applications at large time or length scales or in high-throughput computational workflows (for example, identifying materials with a specific property by screening a database).

In the specific case of pure silica zeolites, i.e., SiO_2 polymorphs, a large number of classical force fields have been used in the literature, with different functional forms or parametrizations. Combariza et al. reviewed various existing interatomic potentials,[1] and highlighted that accurate atomistic molecular dynamics simulations account for a delicate balance of interactions. Yet, at the same time, it is known that a detailed description of the framework dynamics is key in the understanding of the macroscopic behavior of zeolites: many of their properties arise from the interplay between the motions of the framework with an external constraint, which can be a change in temperature, the application of mechanical stress, or the adsorption of guest molecules (in the gas or liquid phase). Computational studies have shown that systematic DFT calculations in the linear response regime under the application of pressure,[2] or in the quasi-harmonic approximation (QHA),[3] allow the calculation of mechanical and thermal properties of pure-silica zeolites. However, these approaches capture only a fraction of the configuration space of zeolitic frameworks, and the computational cost of the more general ab initio MD approach limits its use.

Machine-learned potentials, or machine learning interatomic potentials (MLIPs), have garnered significant attention in recent years due to their ability to capture complex interatomic interactions with high accuracy as well as their computational efficiency. They are data-driven models, typically deriving the energy and atomic forces of a given molecular configuration through trained neural networks, rather than relying on a physics-informed and parametrized analytical decomposition of the interactions at play. They can achieve an accuracy that is

Received: October 29, 2024
Revised: November 1, 2024
Accepted: November 4, 2024
Published: November 13, 2024

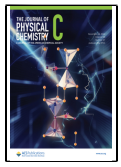

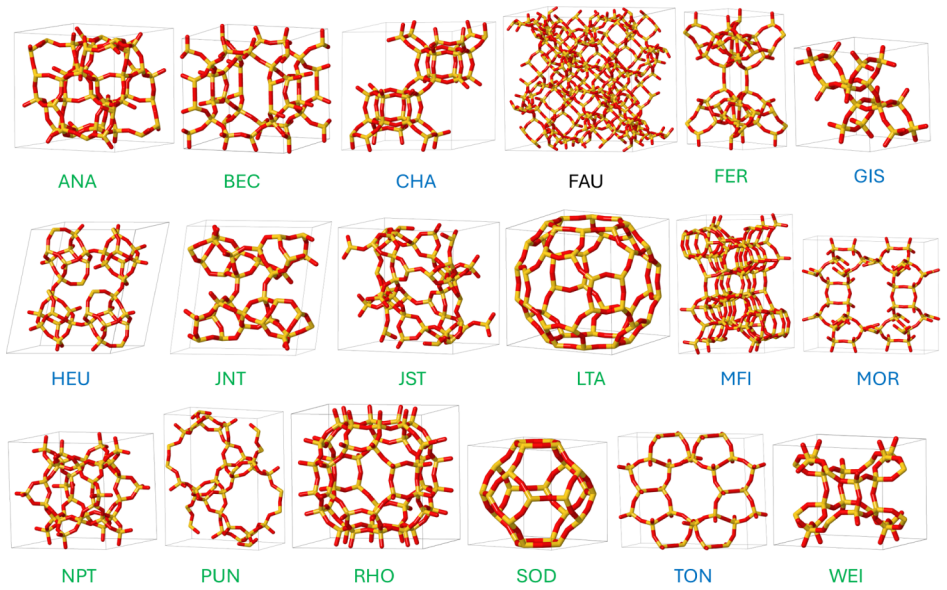

Figure 1. Unit cells and labels of the pure silica zeolite frameworks considered in this work. Green and blue labels are adopted, respectively, for the frameworks used for the training of the potential and for an external validation of the potential. FAU, labeled in black, was used as external validation without ab initio reference data.

close to the reference data that they are trained on while retaining sufficient flexibility to describe chemically and structurally complex environments. Over the past few years, their use has been rapidly growing, and they have been applied to a large and diverse number of systems, ranging from isolated molecules to materials, and from organic bonds to inorganic coordination.[4] They have been very recently used, in particular, to describe silica systems, such as amorphous glasses and zeolites. In this work, we have created and published a data set of trajectories, energies, and forces obtained from high-temperature ab initio molecular dynamics on a diverse set of zeolitic topologies (see Figure 1). Trained on this new large-scale data set, we optimized a machine learning interatomic potential (MLIP) for pure silica zeolites, which we then used to simulate the structure, the thermal expansion properties, and the effects of pressure on a selection of zeolites, both inside and outside its original training set, in order to probe its generalizability.

2. COMPUTATIONAL METHODS

In this section, we provide the key details of the computational procedures followed in the present work. In addition, for full reproducibility of our work, representative input files for all types of calculations performed are made available online at https://github.com/fxcoudert/citable-data.

2.1. DFT Calculations. The ab initio data set used for training the machine learning interatomic potential (MLIP) was generated by periodic DFT calculations using the QUICKSTEP/CP2K software.[5,6] This code makes use of a hybrid basis set formed by Gaussian functions and plane waves, where the wave functions are described by the Gaussian basis with the addition of an auxiliary plane wave basis to describe the density. The strongly constrained and appropriately normed (SCAN) meta-GGA functional[7] was chosen for its good performance across a diverse range of chemical systems and properties of interest. In particular, it reproduces satisfactorily the structural and elastic properties and the relative stability of different silica polymorphs.[8,9] The inner core of Si and O was described by the Goedecker−Teter−Hutter (GTH) type of pseudopotential,[10−12] with triple-ζ valence polarized Gaussian basis sets employed for the valence electrons.

Two types of geometry optimization were performed on the conventional unit cells of the zeolite frameworks considered in this study. In one case, starting from the literature geometries (IZA Structure Commission, Database of Zeolite Structures: https://www.iza-structure.org/databases/), we obtained four distinct distorted cells from each structure, in which the cell parameters varied by −3%, −1.5%, 0%, and +1.5%. In the other case, full optimization of the system was achieved by performing an iterative optimization cycle, alternating between the optimization of internal coordinates and the optimization of cell parameters, until both converged. We found this approach to be more robust in finding the lowest energy structure compared to the simultaneous optimization of both lattice and internal coordinates.

In all of the latter calculations, the SCF convergence threshold was set at 10^{-9} Hartree, while the geometry optimization was considered achieved when maximum atomic forces and atomic displacement were both below 10^{-4} Bohr and 10^{-4} Hartree/Bohr, respectively. QUICKSTEP makes use of a multigrid system to regulate the accuracy of the calculations: four grids with a cutoff of 900 Ry on the main grid and a relative cutoff of 100 Ry were enough to optimize most of the structures and to perform AIMD on them. To fully optimize all the structures, a more accurate multigrid was required, formed by five grids, a main cutoff of 1800 Ry and a relative cutoff of 300 Ry.

2.2. Ab Initio Molecular Dynamics Simulations. In order to generate a diverse and physically representative set of zeolite configurations, we performed ab initio molecular dynamics (AIMD) simulations, coupling Born−Oppenheimer dynamics with the evaluation of the energy and atomic forces at the DFT level. AIMD simulations were run on the four strained structures of each of the 17 zeolite frameworks considered. QUICKSTEP/CP2K, with the same computational setting adopted in the relaxation of the distorted lattices, was employed. The equations of motion were integrated with a time step of 0.5 fs.

https://doi.org/10.1021/acs.jpcc.4c07365
J. Phys. Chem. C 2024, 128, 20512−20522

Table 1. Comparison between the Lattice Parameters and Volume of the Zeolite Frameworks used in the Training Set Obtained from DFT Minimization and MLIP Molecular Dynamic Relaxation

Framework	Method	a (Å)	b (Å)	c (Å)	α (deg)	β (deg)	γ (deg)	V (Å^3)	$\Delta V/V$ (%)
JNT	MLIP	8.231	14.179	13.495	90.00	87.125	90.00	1573	−0.37
	DFT	8.237	14.167	13.602	90.00	87.125	90.00	1579	
NPT	MLIP	13.940	13.940	13.940	90.00	90.00	90.00	2709	−0.45
	DFT	13.961	13.961	13.961	90.00	90.00	90.00	2721	
PUN	MLIP	14.713	8.659	18.972	90.00	90.00	90.00	2417	0.44
	DFT	14.647	8.621	19.058	90.00	90.00	90.00	2406	
WEI	MLIP	11.782	10.260	9.972	90.00	90.00	90.00	1205	−1.79
	DFT	11.919	10.346	9.954	90.00	90.00	90.00	1227	
ANA	MLIP	13.366	13.366	13.367	90.00	90.00	90.00	2388	−0.06
	DFT	13.369	13.369	13.369	90.00	90.00	90.00	2389	
LTA	MLIP	11.826	11.826	11.826	90.00	90.00	90.00	1654	−0.21
	DFT	11.834	11.834	11.834	90.00	90.00	90.00	1657	
JST	MLIP	15.072	15.072	15.072	90.00	90.00	90.00	3424	1.96
	DFT	14.975	14.975	14.975	90.00	90.00	90.00	3358	
FER	MLIP	18.502	13.915	7.336	90.00	90.00	90.00	1888	−0.43
	DFT	18.575	13.926	7.333	90.00	90.00	90.00	1897	
BEC	MLIP	12.643	12.643	12.848	90.00	90.00	90.00	2054	−2.45
	DFT	12.606	12.606	13.250	90.00	90.00	90.00	2106	
SOD	MLIP	8.661	8.661	8.661	90.00	90.00	90.00	649.8	1.52
	DFT	12.606	12.606	13.250	90.00	90.00	90.00	640	
RHO	MLIP	14.524	14.524	14.524	90.00	90.00	90.00	3064	−7.46
	DFT	14.905	14.905	14.905	90.00	90.00	90.00	3311	

The unit cell of the systems was fixed, and the simulations were carried out in the canonical ensemble (N, V, T) at 1000 K, adopting the CSVR[13] thermostat with a time constant of 1 ps to regulate the temperature. Each system was simulated for a duration of 20 ps. Snapshots of each system were sampled every 20 timesteps, resulting in a total of 1000 configurations per strained structure, which were used to build the data set. We found that during the dynamics, for some strained structures, a few configurations could have very large forces, and those outliers would negatively impact the training of the force field. Therefore, configurations with atomic forces higher than 15 eV Å^{-1} were excluded from the data set. Among the 64 considered structures, one was found to exhibit dynamically unstable behavior (the most strained cell of JST), leading to its exclusion from the data set to ensure the integrity and reliability of the training data.

2.3. Interatomic Potential Training. The interatomic potential (IP) was trained with the use of neural equivariant interatomic potentials (NequIP),[14] an equivariant graph neural network approach for learning interatomic potentials from ab initio calculations for molecular dynamics simulations. NequIP represents a significant advance over prior nonequivariant models, by utilizing higher-order tensors instead of relying solely on scalar features. This allows NequIP to capture the complexities of molecular systems more effectively, encoding bond angles, dihedral angles, and other angularly dependent features in a more flexible manner—something of high interest in this work given the strongly directional nature of the interactions. Compared to other deep neural network models, this approach is more efficient, requiring a smaller training set to develop accurate machine-learned interatomic potentials (MLIPs).

The development of the NequIP model depends on several hyperparameters, which determine the accuracy of the potential and the efficiency of the training procedure. In this work, we tuned these hyperparameters to improve the model's performance and sufficiently capture the physics of the systems described. Specifically, before training our final model, we explored the effects of the cutoff radius (r_{max}), which regulates the range of interatomic interactions considered, and the maximum rotational order (L_{max}), which limits the rank of the tensor product considered by NequIP. Additionally, we investigated hyperparameters that impact the learning behavior itself (i.e., the optimization of the ML model): we looked at the influence of the initial learning rate (LR) and the number of interaction blocks in the network on the training speed.

The tuning process involved systematically adjusting the parameters and assessing their effects on the model's accuracy and computational efficiency. In order to avoid overfitting and limit data leakage, this optimization of the hyperparameters was conducted on a subset of the training set, focusing on zeolite frameworks SOD, BEC, and JST. The selected zeolites represent a diverse range of structures in terms of size and density; they range from small (SOD, 36 atoms) to medium (BEC, 96 atoms) and large (JST, 144 atoms) unit cell zeolites and, in density, span from 1.8 g/cm^3 (SOD) to 1.55 g/cm^3 (BEC) and 1.4 g/cm^3 (JST). This also allowed us to restrain the computational load during systematic tests, and efficiently explore a wider range of values for the hyperparameters.

2.4. Classical Molecular Dynamics Simulations. We then used our trained interatomic potential (IP) to perform molecular dynamics (MD) simulations with the LAMMPS code,[15] using the pair_nequip pair style provided by the NequIP developers and available online at https://github.com/mir-group/pair_nequip.

For each zeolite framework, we created a 2 × 2 × 2 supercell based on the crystalline unit cell obtained from the IZA database. The equations of motion were integrated using a time step of 0.5 fs in all simulations. The following procedure was followed for all classical simulations:

https://doi.org/10.1021/acs.jpcc.4c07365
J. Phys. Chem. C 2024, 128, 20512−20522

Table 2. Comparison between the Lattice Parameters and Volume of the Zeolite Frameworks Used in the Evaluation Set Obtained from DFT Minimization and MLIP Molecular Dynamic Relaxation

Framework	Method	a (Å)	b (Å)	c (Å)	α (deg)	β (deg)	γ (deg)	V (Å^3)	$\Delta V/V$ (%)
MOR	MLIP	17.865	20.095	7.381	90.00	90.00	90.00	2650	−0.31
	DFT	17.789	20.173	7.406	90.00	90.00	90.00	2658	
MFI	MLIP	20.024	19.674	13.099	90.00	90.00	90.00	5204	−0.45
	DFT	20.103	19.596	13.211	90.00	90.00	90.00	5228	
GIS	MLIP	9.539	9.539	9.886	90.00	90.00	90.00	900	−0.51
	DFT	9.570	9.570	9.872	90.00	90.00	90.00	904	
CHA	MLIP	9.285	9.285	9.285	93.87	93.87	93.87	795	0.06
	DFT	9.286	9.286	9.286	94.06	94.06	94.06	794	
HEU	MLIP	17.346	17.466	7.326	90.00	116.10	90.00	1993	0.82
	DFT	17.246	17.550	7.310	90.00	116.68	90.00	1977	
TON	MLIP	13.536	17.122	5.044	90	90	90	1169	−1.32
	DFT	14.012	17.114	4.940	90	90	90	1185	

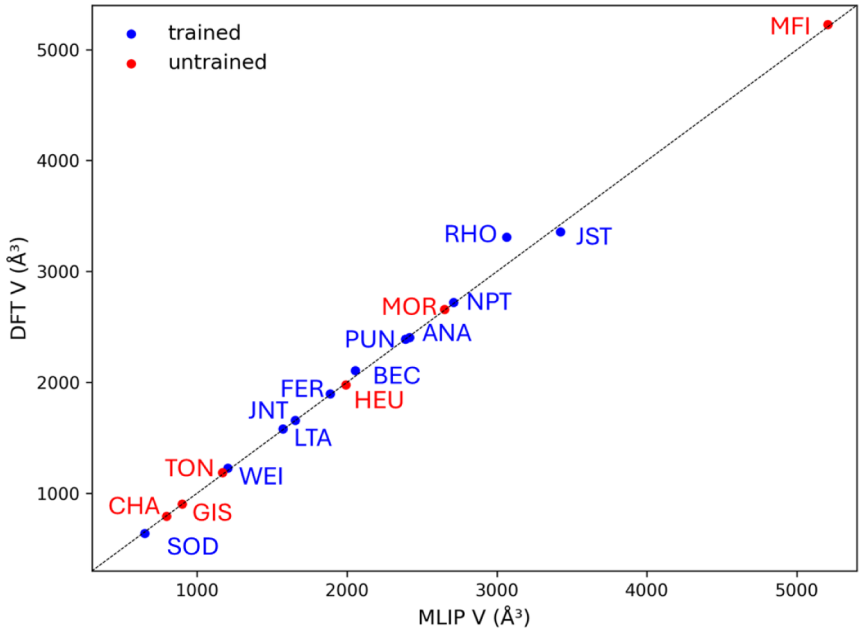

Figure 2. Correlation plot between the relaxed volume computed at the DFT (SCAN) level and with the trained MLIP for the different frameworks used in the training set (blue dots) and as the evaluation set (red dots).

1. Relaxation. Initially, each structure was relaxed through 200 ps of constant pressure (N, P, T) MD simulation at a temperature of 20 K and a pressure of 0 GPa.
2. Temperature ramping. The conditions were then switched to constant volume (N, V, T), and the temperature was gradually increased to the target value over a 10 ps simulation.
3. Equilibration. Subsequently, the conditions were switched back to (N, P, T), and 200 ps of dynamics were performed at the target temperature and pressure.

In all (N, P, T) simulations, pressure and temperature were controlled using the Nosé−Hoover thermostat[16,17] and the Nosé−Hoover barostat,[18] with damping time scales of 50 and 500 fs, respectively. In the (N, V, T) simulations, only the Nosé−Hoover thermostat was employed. For simulations at pressures higher than 1 GPa, the use of a pressure ramping approach would increase the stability of the simulation, allowing the system to reach a higher pressure (from 3 to 10 GPa, depending on the system) almost quasistatically, compared to initializing the system directly at the target pressure (which would fail above the range of 3−4 GPa).

These simulations explored a temperature range between 20 and 900 K for evaluating the thermal properties. Mechanical properties were investigated at 20, 300, and 600 K and in a pressure range of up to 0−10 GPa. Properties of interest were computed as averages from the last 50 ps of each simulation. Furthermore, the elastic constants were computed at 20 K using the ELASTIC_T scripts from LAMMPS, applying a strain of 2% to the simulation box.

The effects of the simulation box size were tested for CHA using unit cells, 2 × 2 × 2, and 3 × 3 × 3 supercells, on both thermal expansion and elastic constants, revealing negligible differences.

3. RESULTS AND DISCUSSION

3.1. Force Field Training and Hyperparameters Tuning. Out of the data sets obtained for the 17 frameworks, 11 were used for training the interatomic potential, while the remaining 6 data sets served as a test set to evaluate the performance of the trained potential and its generalizability across unseen zeolitic topologies—an important quality for the exploration of novel materials. To optimize the potential

https://doi.org/10.1021/acs.jpcc.4c07365
J. Phys. Chem. C 2024, 128, 20512−20522

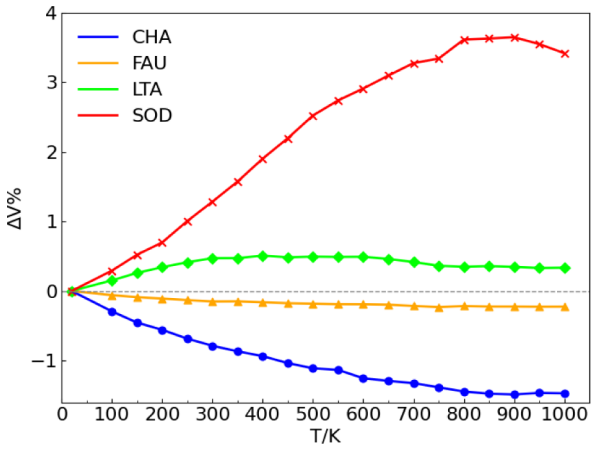

Figure 3. Plot of the percentage variation of the volume with the temperature, between 20 and 1000 K, for the different frameworks considered.

training procedure, a subset of the data set comprising data from SOD, BEC, and JST was selected. This subset comprised a total of 12 300 configurations, which were subsequently divided into 11 100 configurations for training and 1200 configurations for validation in the cross-validation scheme. In all of the training sessions, the loss function was minimized by adopting the same scaled weights on forces and energies.

Hyperparameters such as r_{max} (cutoff radius for interatomic interactions) and L_{max} (maximum rotation order considered by NequIP) were tested and optimized. Other hyperparameters used default values, as suggested by the NequIP developers. As depicted in Figures S1 and S2, increasing r_{max} improves the accuracy of the potential, with convergence reached with fewer iterations. Furthermore, higher accuracies and faster convergences are achieved by increasing the number of layer blocks from 3 (Figure S1) to 5 (Figure S2).

The highest accuracy is obtained with an r_{max} of 6 Å and five layer blocks. However, adopting an r_{max} of 5 Å provides very close accuracy, with an increase of the MAE of the forces from 30.2 to 30.4 meV Å^{-1} and an increase of the MAE of the energy per atom from 0.130 to 0.164 meV. In addition, this choice saves about 20% (22 h) of the total GPU time of the training, which would result in a much more significant GPU time saving on the training of the whole data set, and will result in a more efficient model in production simulations as well.

The results of these tests show that both r_{max} and L_{max} have a significant impact on the final accuracy of the trained model. While a value of r_{max} = 4 Å may intuitively seem large enough to describe the atomic environment around Si and O in a zeolitic framework, we find that larger values of 5 and 6 Å lead to a further improvement of both forces and energies, as shown in Figure S3. Moreover, by increasing the number of interaction layers in the model from 3 to 5, there is an overall improvement in performance, while the differences between models obtained with different r_{max} values are decreased. Given the similar performances of the models with r_{max} = 5 Å and r_{max} = 6 Å, and the lower computational cost of the former, we settled on r_{max} = 5 Å as a compromise for all the following tests.

Another parameter that affects the accuracy of the model is the value of L_{max} which represents the maximum rotation order considered by NequIP. Typically, good results are obtained with a value of 1, while increasing it to 2 can lead to improved accuracy at the expense of speed and memory requirements. In our evaluation, we assessed the balance between the increase in accuracy achieved with a higher L_{max} and the associated increase in computational cost. Based on the training curves depicted in Figure S4, we see that increasing L_{max} to 2 resulted in a modest improvement in the accuracy of the model for forces and energies, with a decrease of approximately 0.9 meV Å^{-1} and 0.04

Table 3. Computed Volumetric and Linear Thermal Expansion Coefficients for Different Temperature Ranges[a]

Zeolite	Temp Range (K) (Exp. Range)	α_V (MK^{-1})	α_a (MK^{-1})	α_b (MK^{-1})	α_c (MK^{-1})
CHA	20−300	−28.12	−14.46	−14.90	1.21
CHA	300−600	−15.67	−6.30	−6.57	−2.79
CHA	600−900	−10.52	−5.34	−14.53	−4.49
CHA	900−1000	−8.24	−2.33	−5.77	−0.21
CHA	20−1000	−16.80	−7.59	−10.81	−1.45
CHA	300−900 (293−873,[32] 308−753[29])	−13.07 (−28.5,[32] −21.22[29])	−5.29 (−8.24,[32] −9.11[29])	−9.79 (−8.24,[32] −9.11[29])	−2.89 (−13.3,[32] −3.08[29])
SOD	20−300	35.87	11.96	11.96	11.96
SOD	300−600	62.83	20.94	20.94	20.94
SOD	600−900	43.57	14.52	14.52	14.52
SOD	900−1000 (1033−1123[24])	−22.11 (−14.0[24])	−7.37 (−4.7[24])	−7.37 (−4.7[24])	−7.37 (−4.7[24])
SOD	20−900	39.72	13.24	13.24	13.24
SOD	20−1000	34.85	11.62	11.62	11.62
LTA	20−300 (100−300[33])	12.34 (−22.1[33])	4.11 (−7.37[33])	4.11 (−7.37[33])	4.11 (−7.37[33])
LTA	300−600	4.92	1.64	1.64	1.64
LTA	600−900	0.10	0.03	0.03	0.03
LTA	900−1000	−3.81	−1.27	−1.27	−1.27
LTA	20−1000	3.20	1.07	1.07	1.07
FAU	20−300 (25−298[30])	−5.40 (−15.8[30])	−1.80 (−2.5[30])	−1.80 (−2.5[30])	−1.80 (−2.5[30])
FAU	20−600 (25−573[30])	−4.93 (−12.6[30])	−1.64 (−4.2[30])	−1.64 (−4.2[30])	−1.64 (−4.2)
FAU	300−600 (298−573)	−0.23 (−13.6)	−0.08 (−4.6)	−0.08 (−4.6)	−0.08 (−4.6)
FAU	300−900 (298−923[31])	−0.76 (−11.8[31])	−0.25 (−4.0[31])	−0.25 (−4.0[31])	−0.25 (−4.0[31])
FAU	900−1100 (923−1123[31])	1.76 (30)	0.59 (10)	0.59 (10)	0.59 (10[31])
FAU	20−1000	−2.33	−0.78	−0.78	−0.78

[a]Experimental values are reported in parentheses for the appropriate temperature range.

https://doi.org/10.1021/acs.jpcc.4c07365
J. Phys. Chem. C 2024, 128, 20512−20522

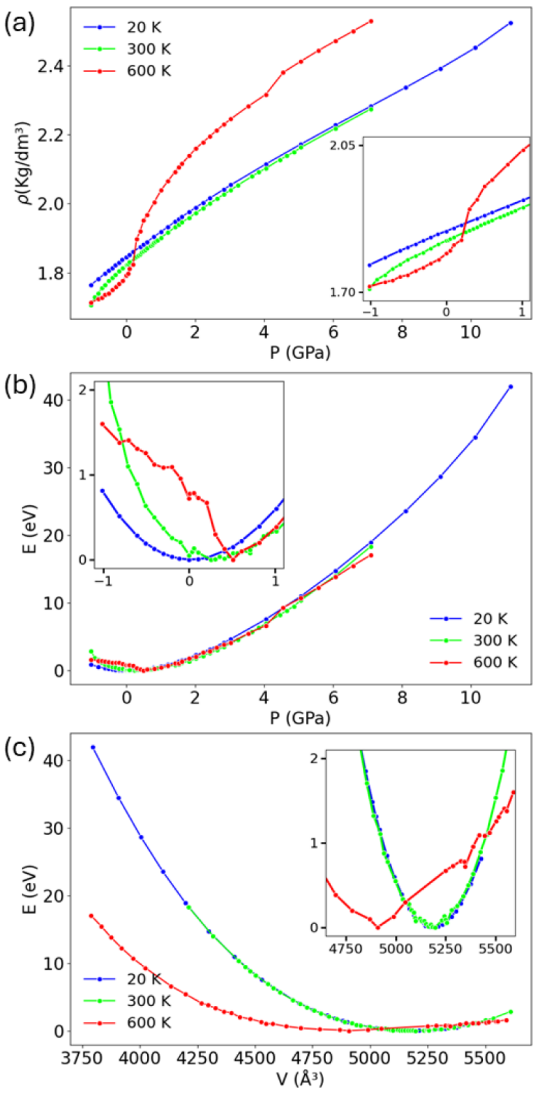

Figure 4. Pressure/density (a), pressure/energy (b), and volume/energy (c) curves for the SOD framework in the −1 to +2 GPa range.

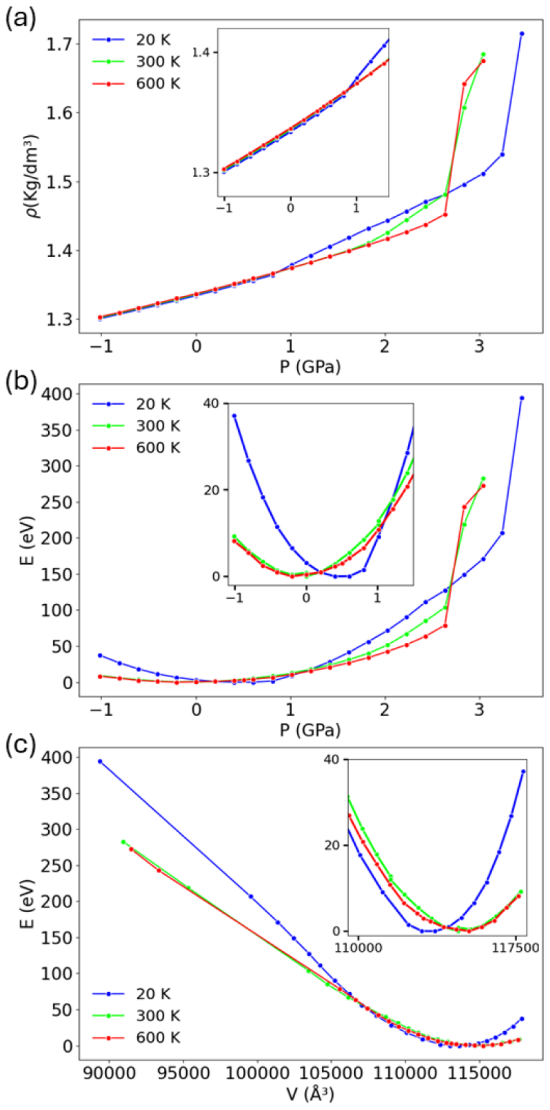

Figure 5. (a) Pressure/density, (b) pressure/energy, and (c) volume/energy curves for the FAU framework in the −1 to +3.5 GPa range.

Table 4. Bulk Modulus and Pressure Derivative of the Bulk Modulus Obtained by Fitting the Third-Order Birch−Murnaghan Equation of States and the Pressure at Which a Transition Was Observed

Framework	T (K)	B_0 (GPa)	B_0'	P_t (GPa)
SOD	20	25.0	3.43	—
	300	24.6	6.94	—
	600	10.0	−7.44	0−0.5
CHA	20	20.0	10.65	1.4
	300	47.4	21.90	1.0
	600	52.1	30.21	0.8−1.0
FAU	20	61.7	13.78	0.8−3.4
	300	45.3	16.40	1.8−3.0
	600	37.0	7.54	2.6−3.0

meV. However, this improvement came at the cost of a significant increase in the simulation time, approximately 90% longer (88 h vs 171 h on our hardware). Additionally, it is worth noting that the MAE of the forces from training and validation diverged in the case of the model with $L_{max} = 2$. Considering the limited improvement in accuracy and the substantial increase in computational cost associated with a higher L_{max} value, we decided to keep it fixed at 1.

Lastly, we also examined the effect of the initial learning rate (LR) used during training. From the tuning test conducted, we concluded that the most balanced set of parameters to use in the training, which included the full data set, would be constituted by $r_{max} = 5$ Å, five interaction blocks, $L_{max} = 1$, and an initial LR = 0.005.

With the selected hyperparameters, the final training was performed on the full set formed by the atomic configurations, atomic forces, and unit cell energies for 41 000 configurations, split into 37 000 and 4000 between training and validation, respectively, from the frameworks ANA, BEC, FER, JNT, JST, LTA, NPT, PUN, RHO, SOD, and WEI. The resulting training and validation curves are reported in Figure S5. Each training task was performed on a single GPU, the NVIDIA V100 Tensor Core GPU. The training of the test models required between 4 and 9 days each, while the training of the final model required 21 days.

All training was originally performed with the main (stable) development branch of NequIP, which does not include the computation of the stress, and the potentials resulting from this

https://doi.org/10.1021/acs.jpcc.4c07365
J. Phys. Chem. C 2024, 128, 20512−20522

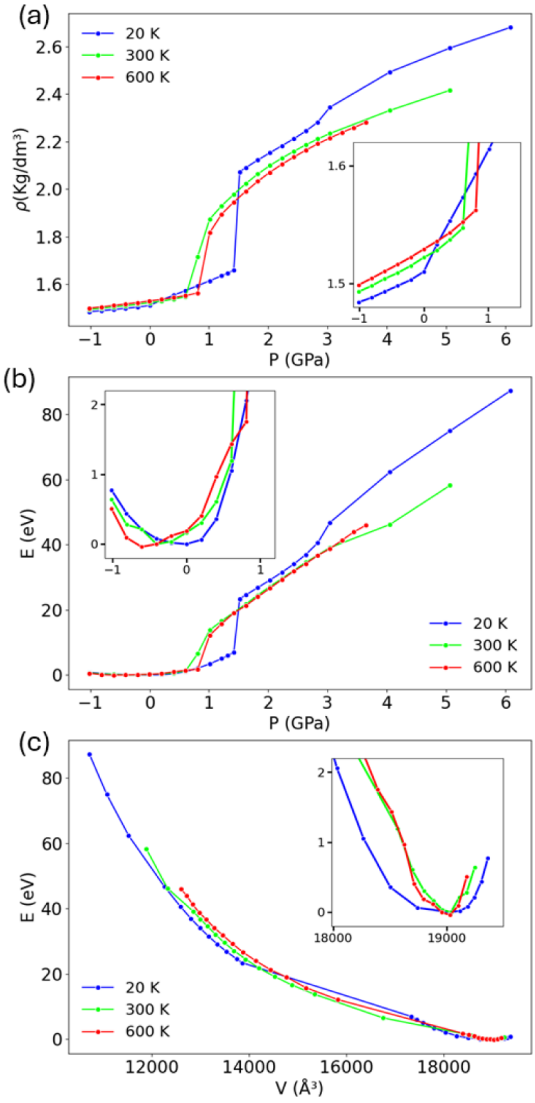

Figure 6. (a) Pressure/density, (b) pressure/energy, and (c) volume/energy curves for the CHA framework in the −1 to +6 GPa range.

branch were unable to describe the volume variation of the zeolites and could not be used in constant-pressure MD simulations. To overcome this shortcoming, the ML potential obtained from the main branch was updated by performing a single step of training adopting the stress-branch version of NequIP, which encoded the evaluation of the virial on the final form of the deployed potential. To check that this update did not mess up the potential, the errors on the training set were computed with both versions, which resulted in negligible differences on all the metrics considered (below the third decimal point).

The training curves obtained on the larger and more diversified training set showed a higher MAE than those obtained from the initial subset, as expected from increasing the heterogeneity of the data set. Nevertheless, the computed errors are well within the range for the MLIPs on siliceous systems.[8,9,19]

3.2. Generalizability of the Potential. The performance of the model was further assessed on the single data set for each zeolite type and on each of the four considered structure deformations. The whole data set exhibited a mean absolute error (MAE) on forces of 32.2 meV Å^{-1}, while for the single framework data sets, the MAE ranges between 29.8 and 34.4

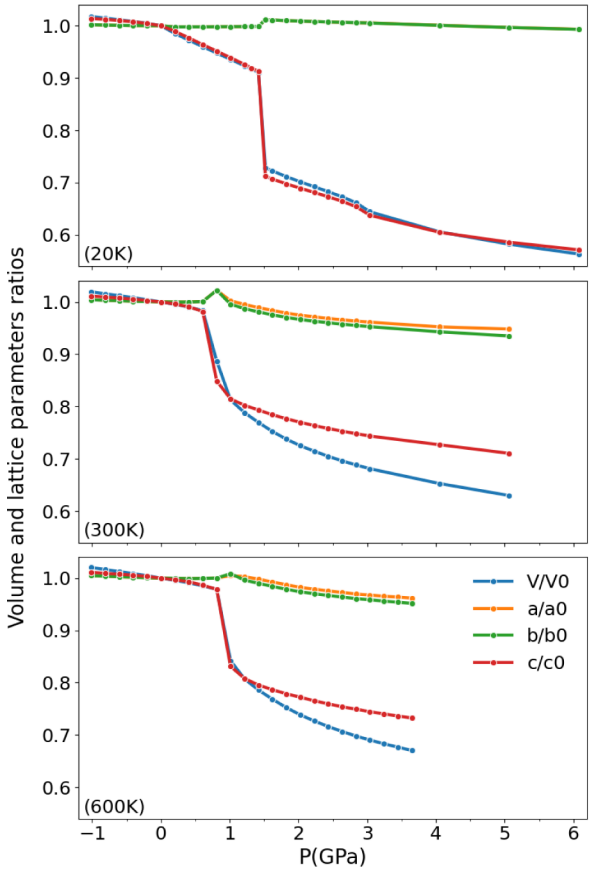

Figure 7. Ratios V_0/V, a_0/a, b_0/b, and c_0/c plotted against the applied pressure for the CHA framework at different temperature values.

meV Å^{-1}. Concerning the errors for the energies per particle, the MAE for the training set is 0.51 meV, while for the single framework data sets, it is 0.46 meV or below, with the exception of JNT and WEI, which have higher MAE values (1.38 and 1.51 meV, respectively). As a comparison, with another MLIP recently developed with DeePMD-kit[20] on pure siliceous zeolites, the reported MAE on forces and energies were respectively 39 meV Å^{-1} and 7.8 meV per particle, on a training set of about 280 000 configurations from AIMD simulations on 219 different topologies from the IZA database.[19] Another work adopted SchNet[21] to train an MLIP adopting both quartz polymorphs, well-known zeolite topologies and zeolites extracted from the Deem database,[22,23] reporting MAE values for energies of 155 meV Å^{-1} and 3.83 meV per particle.[9]

By inspecting the metrics for the data set of each deformed framework, we see that the accuracy may change with the volume of the unit cell, within the same framework type. In most cases, the deformed structures with the largest strain−lowest volume (labeled "2") and with the largest volume (labeled "3") − exhibit the highest and the lowest MAE on the forces, respectively. A similar trend can be observed with the MAE of the energies, although with more fluctuations. Within the two frameworks with the highest MAE, JNT and WEI, the internal differences between the deformed structures are more striking than those in the other case.

The performance of the MLIP on the evaluation data set aligned with that on the training set, showing good generalization, except for the TON framework, which displays MAEs on forces and energy per particle that are respectively 4−5 times and 40−80 times higher than those on the training set,

https://doi.org/10.1021/acs.jpcc.4c07365
J. Phys. Chem. C 2024, 128, 20512−20522

indicating it as a possible outlier. The collected metrics computed on the training and on the evaluation training set are reported in Tables S1 and S2.

The trained MLIP was then assessed for the prediction of the lattice parameters of different zeolitic frameworks, where crystal shapes were constrained in both static DFT and MD simulations. Tables 1 and 2 report the comparison between the results of the two methods. We observe that unit cell volumes are predicted with an MAE of 1.21%, considering structures from both the training and test sets, while errors lower than 0.5% were achieved for 8 out of the 17 frameworks. This displays better accuracy than empirical zeolite force fields used in the field, indicating the advantage of the ab initio data-based force field optimization.

Figure 2 shows the DFT and MLIP computed equilibrium volumes for the different frameworks, including both the training and evaluation sets. We note here that the cubic system RHO exhibited the largest deviation from the DFT results, with a volume deviation of 7.46%. This is a special (and interesting) case because DFT optimization revealed two local minima structures with different volumes, while the MD relaxation resulted in a structure with a volume close to the metastable, low-volume configuration. Despite this complication, the trained MLIP demonstrated reasonably accurate performance, considering it was trained solely on high-energy structures without specific consideration of the energy minima.

3.3. Thermal Expansion Simulations. Understanding the thermal expansion behavior of zeolites has important implications for practical applications, in part for process engineering, but also because the diffusivity and reactivity of the guest molecules in the structure are strongly influenced by the size of the pores, which can contract or expand with variations in temperature.

Zeolites are known to be one of the few classes of materials that can feature negative thermal expansion (NTE), where the material contracts upon heating, a difference from most materials that expand upon heating. In zeolites, as in some other framework materials, the NTE behavior has been attributed to the presence of rigid unit modes (RUMs) originating from their corner-sharing tetrahedral structure. When heated, these RUMs permit the "flexing" or rotation of these tetrahedral units within the zeolitic framework, causing an overall contraction of the material, and thereby leading to NTE. Essentially, the thermal energy allows the rotation of the corner-sharing tetrahedra, resulting in a smaller overall volume even as the temperature rises. Both experimental and in-silico investigations found exceptions to this behavior, i.e., zeolites with positive thermal expansions (PTE), but since their rarity and the presence of RUMs in all of these frameworks, it is still debated that PTE in these systems is due to the nanoporous nature of the material instead of the framework itself.

The characterization of the thermal behavior of zeolites is made experimentally difficult by the combination of several factors. First, the analysis of thermal expansion requires the presence of single-crystal data, which are difficult to obtain on fully evacuated/activated samples; in some cases in the literature, organic templates or solvent molecules are still present in the pores, which affects the thermal behavior. Second, several zeolitic frameworks undergo phase transitions upon heating, which makes their thermal expansion harder to analyze. Therefore, the computational study of the thermal behavior of zeolites is an area of active research. In a previous work by our group, the thermal expansion coefficient of the pure-silica zeolites was systematically computed through DFT in the quasi-harmonic approximation (QHA),[3] i.e., in a low-temperature regime, finding that all the investigated frameworks displayed NTE within the temperature range of 10−300 K. The exploitation of DFT and QHA to investigate the thermal properties of the whole zeolitic database is a very demanding task from a computational point of view; therefore, an alternative, cheaper, and as accurate approach is desired. The MLIP was trained on trajectories at different volumes and degrees of strain; therefore, the rotation of the RUMs should be captured by the model.

We investigated the thermal expansion behavior of pure-silica zeolite frameworks, FAU, CHA, LTA, and SOD, through a series of NPT simulations ranging from 20 to 1000 K. We note that volume fluctuations during the MD increase with the temperature, making the results less reliable at the higher end of the temperature range. The thermal expansion curves and computed thermal expansion coefficients are reported respectively in Figure 3 and Table 3, and we now discuss them individually against the known experimental data.

SOD: sodalite shows positive thermal expansion (PTE) up to 800 K, then expansion stops and starts to contract between 900 and 1000 K, in apparent agreement with observations which found the inversion of the expansion behavior at about 700 K.[24,25] It must be noted that while experimental measurements found a PTE for sodalite minerals in this wide range of T,[26] the study of Leardini et al.[24] found for pure silica sodalite PTE between 273 and 573 K and NTE above 653 K. These differences were ascribed to the neutral nature of the organic template they used in the synthesis, which once calcinated did not interfere with the framework, allowing the contraction of the structure.

LTA: for the pure-silica LTA zeolite (experimentally called ITQ-29), PTE was observed from 20 to 400 K; then the volume is stationary in the range of 400−600 K, followed by NTE from 600 to 1000 K. Unfortunately, the only experimental results reported on the thermal expansion of LTA are limited to the low-temperature regime, between 100 and 300 K, where a strong NTE was observed, with a mean thermal expansion coefficient (300 to 100 K) of -22.1×10^{-6} K^{-1}.[27] At this stage, it is unclear whether the origin of this discrepancy at low temperature comes from an inadequacy of the MLIP (which was trained mostly on high-temperature data) or from the DFT calculations themselves.

CHA: for chabazite, NTE is found for the whole T range explored and shows the largest (negative) thermal expansion coefficient α_V among the investigated frameworks, -13.07×10^{-6} K^{-1} between 300 and 900 K, in qualitative agreement with the experimental value (-28.5×10^{-6} K^{-1}).[28,29] Different from the experiments, simulations revealed a larger expansion rate at low temperature. Moreover, CHA, being a noncubic framework, has an anisotropic expansion.

FAU: for pure-silica faujasite, NTE is observed up to 900 K, but it is about an order of magnitude lower than CHA in the 20−900 K range, in agreement with experiments.[30,31] Above 900 K, the behavior changes to PTE.

3.4. Isothermal Compression Simulations: Phase Transition and Amorphization. Due to their high porosity, zeolites undergo very important structural changes in response to the application of mechanical pressure. There are several examples of phase transitions involving tilting of the constituent tetrahedra or changes in the ring structures. Pressure may also induce pore collapse and a transition to an amorphous state,

https://doi.org/10.1021/acs.jpcc.4c07365
J. Phys. Chem. C 2024, 128, 20512−20522

which can retain some topological order from the parent crystalline phase and is distinct from common silicate glasses.

We investigated the structural effects of compression on the frameworks SOD, CHA, and FAU through a series of (N, P, T) simulations at increasing values of applied pressure. The influence of temperature was evaluated by performing these series of simulations at 20, 300, and 600 K. The range of pressure investigated shows a variation in the cell volume that can exceed that imposed on the structure for the generation of the training data (i.e., between +1.5% and −3.0%). We also performed calculations of the second-order elastic tensor at 20 K in order to demonstrate the potential for the MLIP to describe anisotropic mechanical properties and to investigate the influence of system size by comparing 2 × 2 × 2 supercells and 3 × 3 × 3 supercells. These results are reported and discussed in the Supporting Information.

SOD: the mechanical properties of siliceous sodalite were experimentally found to be significantly influenced by the nature of the contained template species, even in cases of supposedly weak interactions.[34−37] For instance, the experimental bulk modulus B_0 ranges between 24 GPa[37] and 132 GPa.[36] This variability is justified by the existence of two low-pressure phases with different compressibilities, whose relative stability at ambient pressure is influenced by the template species. Ab initio investigations at the PW91 DFT level on ideal, template-free silica sodalite found that the zero-pressure phase belongs to the high symmetry $Im\bar{3}m$ space group and undergoes a phase transition at 0.12 GPa to the $I\bar{4}3m$ group, with a loss of inversion symmetry.[38] Additionally, two other phase transitions were identified with further compression up to about 4 GPa, preserving the lattice symmetry of $I\bar{4}3m$. The $I\bar{4}3m$ phase was found to be less compressible, with a computed bulk modulus of 113 GPa, closely resembling the experimental value of ∼132 GPa. The three high-pressure $I\bar{4}3m$ phases became progressively more compressible with the bulk modulus decreasing from 67 to 15 GPa. However, the agreement with experimental results is only partial: for example, in the case of dioxolane silica SOD, a transition from cubic to rhombohedral was observed at pressures higher than 1.2 GPa, with the trigonal space group being either $R3m$ or $R3$.[37] This discrepancy with the ab initio calculations is likely due to the constraints adopted in the simulations, which preserved the cubic symmetry of the lattice. All of the studies indicated the increase in the tilting of the silica tetrahedra as the main mechanism of compression underlying the phase-transition $Im\bar{3}m/I\bar{4}3m$, which is supposed to be continuous. On all-silica SOD, pressure-induced amorphization has not been reported in any experimental work.

Our simulation studies found that the behavior of sodalite under pressure changes with temperature: no phase transitions were observed at 20 K in the whole range of P explored (from −1 to 10 GPa), and the structure of minima is located very close to zero pressure, as shown in Figure 4. Similar results were found at 300 K, with the minima structure shifted to about 0.2 to 0.3 GPa. At 600 K, the low-pressure part of the PES curve is difficult to interpret, but a continuous transformation is observed below 0.5 GPa, with a decrease of volume of about 8% (the experimental one of dioxolane silica sodalite in the same P range at 300 K is 3%).[37] No further transitions were found at higher pressure: the isotropic constraints adopted in these simulations prevent the breaking of the lattice symmetry and, thus preventing the observation of the experimentally characterized cubic to rhombohedral transition. A recent work that used the consistent valence force field characterized the pressure-induced amorphization of SOD at 300 K, finding it occurring as a discontinuous transition at 6.81 GPa.[39]

As shown in Table 4, the bulk modulus at 20 and 300 K (obtained through the third-order Birch−Murnaghan equation of state, see Methods) are very close, 25.0 and 24.6 GPa, whereas at 600 K, it decreases to 10.0 GPa. The computed low-temperature values are a good match for the experimental values obtained for the lower symmetry $I\bar{4}3m$ phase rather than the ground state, larger, $Im\bar{3}m$ phase. The negative value of B_0' at 600 K underlines the characterized low-pressure phase transition.

FAU: the experimental characterization under pressure of the purely siliceous faujasite is quite limited. One work investigated the effect of pressure on the IR spectra of the highly siliceous zeolite Y (Si:Al = 100), finding a phase transition from about 1.7 to 2.2 GPa associated with the amorphization of the network.[40] The hypothesized mechanism of amorphization involves primarily the deformation of the double six-membered rings forming the sodalite cages in the network, up to rupture or severe distortion.

Another work characterized the elastic properties of a pure siliceous faujasite, deriving a bulk modulus B_0 of 38 GPa, the same as α-quartz, and the start of amorphization at 2.2 GPa.[41] Our simulations revealed a temperature-dependent relationship between the onset pressure of amorphization and the pressure range within which it occurs, as shown in Figure 5. At 20 K, amorphization initiates between 0.8 and 3.2 GPa; beyond this pressure, the structure collapses, resulting in a 10% volume reduction, followed by unstable dynamics upon further pressure increases. At 300 K, amorphization occurs within a narrower pressure range of 1.8−2.6 GPa, preceding structural collapse. At 600 K, the transition appears to take place between 2.4 and 2.6 GPa, just before structure collapse. The computed B_0 values, fitted between −1 and 1.6 GPa, showed an increasing compressibility of the zeolite with T, from 61.74 to 45.33 to 37.03 GPa in the range of 20 to 600 K, with the latter values in good agreement with the experimental value.

CHA: the experimental characterization of the pure silica chabazite under pressure has found a phase transition at room temperature from the rhombohedral space group $R\bar{3}m$ to the triclinic $P\bar{1}$ occurring at 1.42 GPa.[42] The triclinic symmetry of the cell is preserved up to 3.47 GPa, and then complete, irreversible amorphization is reached at 5.33 GPa.

The simulation results for chabazite under pressure revealed a phase transition within the 0.8 to 1.4 GPa range (Figure 6). In the case of CHA, temperature influences the processes, albeit with a more complex interpretation due to the anisotropic structure. As depicted in Figure 7, at 20 K, compressibility shifts from negative to positive strain, with compression affecting solely the c-axis contraction of the hexagonal cell until reaching the phase transition at 1.4 GPa. This transition is characterized by a volume decrease of approximately 15% and a reduction in the c-axis, accompanied by a minor expansion of lattice parameters a and b, indicative of auxetic behavior. Beyond this pressure, the structure continues to contract predominantly along the c-axis, leading to simulation failure at pressures exceeding 6 GPa. Similarly, at higher T, volume contracts prior to the phase transition, occurring between 0.6 and 1.0 GPa at 300 K, and between 0.8 and 1.0 GPa at 600 K, predominantly affecting the c-axis. Post-transition, the a and b lattice parameters slightly increase, yet under additional stress they exhibit more significant contraction than at lower temperatures. The calculated value of B_0 indicates a reduction in compressibility

https://doi.org/10.1021/acs.jpcc.4c07365
J. Phys. Chem. C 2024, 128, 20512−20522

with increasing temperature, but no experimental data are available on this for comparison.

4. CONCLUSIONS

In this work, we developed a machine learning interatomic potential (MLIP) for pure silica zeolites trained on a diverse set of high-temperature ab initio molecular dynamics data encompassing various zeolitic topologies. The MLIP was successfully utilized to simulate the structure, thermal expansion properties, and the effects of pressure on selected zeolites, demonstrating high accuracy and transferability. Notably, the ability of the MLIP to generalize to other zeolitic frameworks was confirmed by its accurate performance on zeolite structures not included in the training set, indicating its potential applicability to a wide range of pure silica zeolite frameworks. The generalizability of our MLIP suggests a promising path for the exploration and development of novel zeolitic materials, with broad implications for the chemical industry and the nanoporous materials modeling community. Indeed, molecular dynamics simulations of zeolites are commonly employed for the characterization of their framework dynamics and response to the application of temperature and pressure, but existing classical interatomic potentials can only describe interactions with limited accuracy, while density functional theory, meanwhile, is accurate but has a very high computational cost. The use of MLIP offers an interesting middle-ground choice in the computational toolbox of materials scientists and physical chemists. This will allow, in future work, to revisit the questions of high-throughput screening of zeolites for energetic, mechanical, and thermal stability, as well as the question (still widely open) of the experimental feasibility of zeolitic frameworks.

■ ASSOCIATED CONTENT

Supporting Information

The Supporting Information is available free of charge at https://pubs.acs.org/doi/10.1021/acs.jpcc.4c07365.

Error metrics evaluated with the MLIP on the different zeolite subsets and the full set (Tables S1 and S2); elastic constants and related properties (Tables S3 and S4); training and validation curves (Figures S1, S2, S4, and S5); comparison of the normalized time, epochs and MAE (Figure S3); parity plots (Figure S6); thermal expansion plot for LTA (Figure S7); the Birch−Murnaghan equation of states (Figures S8−S10); density of CHA (Figure S11); thermal expansion behaviour of LTA; elastic property calculations; influence of system size (PDF)

■ AUTHOR INFORMATION

Corresponding Authors

Luca Brugnoli − *Chimie ParisTech, PSL University, CNRS, Institut de Recherche de Chimie Paris, Paris 75005, France*; Email: luca.brugnoli1190@gmail.com

François-Xavier Coudert − *Chimie ParisTech, PSL University, CNRS, Institut de Recherche de Chimie Paris, Paris 75005, France*; orcid.org/0000-0001-5318-3910; Email: fx.coudert@chimieparistech.psl.eu

Author

Maxime Ducamp − *Chimie ParisTech, PSL University, CNRS, Institut de Recherche de Chimie Paris, Paris 75005, France*

Complete contact information is available at: https://pubs.acs.org/10.1021/acs.jpcc.4c07365

Notes

The authors declare no competing financial interest.

■ ACKNOWLEDGMENTS

This work was supported by the Agence Nationale de la Recherche (project MATAREB, ANR-18-CE29-0009-01), and access to HPC platforms was provided by a GENCI grant (A0170807069).

■ REFERENCES

(1) Combariza, A. F.; Gomez, D. A.; Sastre, G. Simulating the Properties of Small Pore Silicazeolites Using Interatomic Potentials. *Chem. Soc. Rev.* **2013**, *42* (1), 114−127.

(2) Coudert, F.-X. Systematic Investigation of the Mechanical Properties of Pure Silica Zeolites: Stiffness, Anisotropy, and Negative Linear Compressibility. *Phys. Chem. Chem. Phys.* **2013**, *15* (38), 16012.

(3) Ducamp, M.; Coudert, F.-X. Systematic Study of the Thermal Properties of Zeolitic Frameworks. *J. Phys. Chem. C* **2021**, *125* (28), 15647−15658.

(4) Mortazavi, B.; Silani, M.; Podryabinkin, E. V.; Rabczuk, T.; Zhuang, X.; Shapeev, A. V. First-Principles Multiscale Modeling of Mechanical Properties in Graphene/Borophene Heterostructures Empowered by Machine-Learning Interatomic Potentials. *Adv. Mater.* **2021**, *33* (35), 2102807.

(5) Kühne, T. D.; et al. CP2K: An Electronic Structure and Molecular Dynamics Software Package - Quickstep: Efficient and Accurate Electronic Structure Calculations. *J. Chem. Phys.* **2020**, *152* (19), 194103.

(6) Lippert, G.; Hutter, J.; Parrinello, M. A Hybrid Gaussian and Plane Wave Density Functional Scheme. *Mol. Phys.* **1997**, *92* (3), 477−487.

(7) Sun, J.; Ruzsinszky, A.; Perdew, J. P. Strongly Constrained and Appropriately Normed Semilocal Density Functional. *Phys. Rev. Lett.* **2015**, *115* (3), 036402.

(8) Erhard, L. C.; Rohrer, J.; Albe, K.; Deringer, V. L. A Machine-Learned Interatomic Potential for Silica and Its Relation to Empirical Models. *npj Comput. Mater.* **2022**, *8* (1), 90.

(9) Erlebach, A.; Nachtigall, P.; Grajciar, L. Accurate Large-Scale Simulations of Siliceous Zeolites by Neural Network Potentials. *npj Comput. Mater.* **2022**, *8* (1), 174.

(10) Goedecker, S.; Teter, M.; Hutter, J. Separable Dual-Space Gaussian Pseudopotentials. *Phys. Rev. B* **1996**, *54* (3), 1703−1710.

(11) Hartwigsen, C.; Goedecker, S.; Hutter, J. Relativistic Separable Dual-Space Gaussian Pseudopotentials from H to Rn. *Phys. Rev. B* **1998**, *58* (7), 3641−3662.

(12) Krack, M. Pseudopotentials for H to Kr Optimized for Gradient-Corrected Exchange-Correlation Functionals. *Theor. Chem. Acc.* **2005**, *114* (1−3), 145−152.

(13) Bussi, G.; Donadio, D.; Parrinello, M. Canonical Sampling through Velocity Rescaling. *J. Chem. Phys.* **2007**, *126* (1), 014101.

(14) Batzner, S.; Musaelian, A.; Sun, L.; Geiger, M.; Mailoa, J. P.; Kornbluth, M.; Molinari, N.; Smidt, T. E.; Kozinsky, B. E(3)-Equivariant Graph Neural Networks for Data-Efficient and Accurate Interatomic Potentials. *Nat. Commun.* **2022**, *13* (1), 2453.

(15) Thompson, A. P.; Aktulga, H. M.; Berger, R.; Bolintineanu, D. S.; Brown, W. M.; Crozier, P. S.; in 't Veld, P. J.; Kohlmeyer, A.; Moore, S. G.; Nguyen, T. D.; et al. LAMMPS, - a Flexible Simulation Tool for Particle-Based Materials Modeling at the Atomic, Meso, and Continuum Scales. *Comput. Phys. Commun.* **2022**, *271*, 108171.

(16) Nosé, S. A Unified Formulation of the Constant Temperature Molecular Dynamics Methods. *J. Chem. Phys.* **1984**, *81* (1), 511−519.

(17) Hoover, W. G. Canonical Dynamics: Equilibrium Phase-Space Distributions. *Phys. Rev. A* **1985**, *31* (3), 1695−1697.

(18) Melchionna, S.; Ciccotti, G.; Lee Holian, B. Hoover *NPT* Dynamics for Systems Varying in Shape and Size. *Mol. Phys.* **1993**, *78* (3), 533−544.

(19) Sours, T. G.; Kulkarni, A. R. Predicting Structural Properties of Pure Silica Zeolites Using Deep Neural Network Potentials. *J. Phys. Chem. C* **2023**, *127* (3), 1455−1463.
(20) Wang, H.; Zhang, L.; Han, J.; Weinan, E. DeePMD-Kit: A Deep Learning Package for Many-Body Potential Energy Representation and Molecular Dynamics. *Comput. Phys. Commun.* **2018**, *228*, 178−184.
(21) Schütt, K. T.; Arbabzadah, F.; Chmiela, S.; Müller, K. R.; Tkatchenko, A. Quantum-Chemical Insights from Deep Tensor Neural Networks. *Nat. Commun.* **2017**, *8* (1), 13890.
(22) Pophale, R.; Cheeseman, P. A.; Deem, M. W. A Database of New Zeolite-like Materials. *Phys. Chem. Chem. Phys.* **2011**, *13* (27), 12407−12412.
(23) *Michael Deem's PCOD and PCOD2 Databases of Zeolitic Structures*; Zenodo, DOI: 10.5281/zenodo.4030231.
(24) Leardini, L.; Martucci, A.; Cruciani, G. The Unusual Thermal Expansion of Pure Silica Sodalite Probed by in Situ Time-Resolved Synchrotron Powder Diffraction. *Microporous Mesoporous Mater.* **2012**, *151*, 163−171.
(25) Zheng, Z.; Guliants, V. V.; Misture, S. Sodalites as Ultramicroporous Frameworks for Hydrogen Separation at Elevated Temperatures: Thermal Stability, Template Removal, and Hydrogen Accessibility. *J. Porous Mater.* **2009**, *16* (3), 343−347.
(26) Taylor, D. The Thermal Expansion of the Sodalite Group of Minerals. *Mineral. Mag. J. Mineral. Soc.* **1968**, *36* (282), 761−769.
(27) Carey, T.; Corma, A.; Rey, F.; Tang, C. C.; Hriljac, J. A.; Anderson, P. A. The Effect of Extra Framework Species on the Intrinsic Negative Thermal Expansion Property of Zeolites with the LTA Topology. *Chem. Commun.* **2012**, *48* (47), 5829.
(28) Woodcock, D. A.; Lightfoot, P.; Villaescusa, L. A.; Díaz-Cabañas, M.-J.; Camblor, M. A.; Engberg, D. Negative Thermal Expansion in the Siliceous Zeolites Chabazite and ITQ-4: A Neutron Powder Diffraction Study. *Chem. Mater.* **1999**, *11* (9), 2508−2514.
(29) Martínez-Iñesta, M. M.; Lobo, R. F. Investigation of the Negative Thermal Expansion Mechanism of Zeolite Chabazite Using the Pair Distribution Function Method. *J. Phys. Chem. B* **2005**, *109* (19), 9389−9396.
(30) Attfield, M. P. Strong Negative Thermal Expansion in Siliceous Faujasite. *Chem. Commun.* **1998**, No. 5, 601−602.
(31) Leardini, L.; Quartieri, S.; Vezzalini, G.; Arletti, R. Thermal Behaviour of Siliceous Faujasite: Further Structural Interpretation of Negative Thermal Expansion. *Microporous Mesoporous Mater.* **2015**, *202*, 226−233.
(32) Lightfoot, P.; Woodcock, D. A.; Maple, M. J.; Villaescusa, L. A.; Wright, P. A. The Widespread Occurrence of Negative Thermal Expansion in Zeolites. *J. Mater. Chem.* **2001**, *11* (1), 212−216.
(33) Carey, T.; Tang, C. C.; Hriljac, J. A.; Anderson, P. A. Chemical Control of Thermal Expansion in Cation-Exchanged Zeolite A. *Chem. Mater.* **2014**, *26* (4), 1561−1566.
(34) Braunbarth, C. M.; Behrens, P.; Felsche, J.; van de Goor, G. Phase Transitions and Thermal Behaviour of Silica Sodalites. *Solid State Ionics* **1997**, *101*−*103*, 1273−1277.
(35) Werner, S.; Barth, S.; Jordan, R.; Schulz, H. Single Crystal Study of Sodalite at High Pressure. *Z. Kristallogr. -Cryst. Mater.* **2010**, *211* (3), 158−162.
(36) Fütterer, K.; Depmeier, W.; Altorfer, F.; Behrens, P.; Felsche, J. Compression Mechanism in Trioxane Silica Sodalite, $[Si_{12}O_{24}] \cdot 2\ C_3H_6O_3$. *Z. Kristallogr. -Cryst. Mater.* **1994**, *209* (6), 517−523.
(37) Knorr, K.; Braunbarth, C. M.; Van De Goor, G.; Behrens, P.; Griewatsch, C.; Depmeier, W. High-Pressure Study on Dioxolane Silica Sodalite $(C_3H_6O_2)_2[Si_{12}O_{24}]$—Neutron and X-Ray Powder Diffraction Experiments. *Solid State Commun.* **2000**, *113* (9), 503−507.
(38) Knorr, K.; Winkler, B.; Milman, V. Compression Mechanism of Cubic Silica Sodalite $[Si_{12}O_{24}]$: A First Principles Study of the $Im\bar{3}m$ to $I\bar{4}3m$ Phase Transition. *Z. Kristallogr. -Cryst. Mater.* **2001**, *216* (9), 495−500.
(39) Li, N.; Shi, Z.; Zhai, S.; Zhou, N.; Zhang, P.; Arramel, A.; Bennett, T. D.; Yue, Y. Unveiling the Amorphization of Sodalite Topology Zeolitic Imidazolate Frameworks and Zeolites by Pressure and Stress. *J. Am. Ceram. Soc.* **2023**, *106* (10), 6117−6129.
(40) Havenga, E. A.; Huang, Y.; Secco, R. A. An Investigation of the Effect of High Pressure on the Structure of Siliceous Zeolite Y. *Mater. Res. Bull.* **2003**, *38* (3), 381−387.
(41) Colligan, M.; Forster, P. M.; Cheetham, A. K.; Lee, Y.; Vogt, T.; Hriljac, J. A. Synchrotron X-Ray Powder Diffraction and Computational Investigation of Purely Siliceous Zeolite Y under Pressure. *J. Am. Chem. Soc.* **2004**, *126* (38), 12015−12022.
(42) Confalonieri, G.; Quartieri, S.; Vezzalini, G.; Tabacchi, G.; Fois, E.; Daou, T. J.; Arletti, R. Differential Penetration of Ethanol and Water in Si-Chabazite: High Pressure Dehydration of Azeotrope Solution. *Microporous Mesoporous Mater.* **2019**, *284*, 161−169.